Supporting Information

Li et al. 10.1073/pnas.1218986110

SI Text

Functionally Relevant Molecular Events That Triggered the Structural Changes Accompanying the Formation of Water-Conducting States. Formation of water-conducting states in most of the transporters reported in the present study was accompanied by global conformational changes in the protein structure, which were in turn following specific molecular events either spontaneously taking place during the equilibrium simulations or specifically induced by the initial modeling of the simulation system. These molecular events, which are described below in more detail for each specific system, are all relevant steps in the transport cycle of the respective transporter, and therefore, the resulting structural changes induced by them are also likely representative of structural transitions relevant to the cycle. Although the limited timescale of the simulations prevented us from observing the transition from one major state to another in its entirety, we believe that during these simulations we have been able to capture the early stages associated with such structural transitions. We also note that in all cases, control simulations, i.e., those performed in the absence of the specific triggering molecular events, did not result in the formation of water-conducting states, indicating that the observed phenomenon is not a artifactual protein deformation, e.g., due to simulation conditions. In this section, we describe in more detail these triggering molecular events for each individual membrane transporter reported in the main text. Note that the formation of a water-conducting state in Na^+-coupled glucose transporter (vSGLT) did not rely on such global structural changes and required only structural fluctuations at the level of side chains lining the lumen of the transporter. We, therefore, do not need to further discuss the behavior of this protein in this section.

Na^+ unbinding in benzyl hydantoin transporter, Mhp1. The majority of water permeation events in Mhp1 are preceded by a large-scale conformational change, which is induced by a functionally relevant event—namely, spontaneous unbinding of the Na^+ ion from its binding site. The 1.2-μs equilibrium simulation of Mhp1 (hereafter referred to as Traj 1; Fig. 3), is initiated from the substrate-free, Na^+-bound outward-facing (OF) state (PDB ID code 2JLN) (1). Mhp1 function is known to be Na^+ dependent (1). It has been recently reported that the cotransported Na^+ ion plays a critical role in controlling the protein conformational state in leucine transporter (LeuT)-fold transporters (2, 3), which is the fold adopted by Mhp1. During the simulation, the Na^+ ion present in the starting crystal structure spontaneously unbinds from its original binding site and diffuses into the extracellular side after 600 ns (Fig. S1). Note that the affinity of Na^+ for Mhp1 in the substrate-free state is not high (K_d 1.15 + 0.28 mM) (1). Following Na^+ unbinding, Mhp1 undergoes large-scale conformational changes (Fig. S1), which lead to a transient water-conducting state (Fig. 3).

To verify the effect of Na^+ on structural stability of Mhp1 in the OF state, an independent simulation (Traj 2) was performed starting from the same state as in Traj 1, but with the Na^+ ion constrained to remain in its binding site. During the simulation, the structure remains stable as indicated by lower rmsd (rmsd < 1.8 Å; Fig. S1), and no water-conducting state is observed.

ATP removal in maltose transporter. The water permeability exhibited in the simulations of the maltose transporter is a consequence of the designed OF-to-inward facing (IF) conformational transition. Crystal structures of the maltose transporter have been resolved for multiple states (4–7), and the OF state can only be obtained when the nucleotide binding domains (NBDs) are dimerized in the presence of ATP analogs (4, 6, 7). The removal of the bound nucleotides from the OF structure (PDB ID code 2R6G) (4) was used here as a method to induce rapid NBD dimer opening (more efficient than ATP hydrolysis), and thereby to trigger the conformational changes toward the IF state. Conformational changes in the absence of nucleotides have been captured in isolated NBD structures (8), and in MD simulations of isolated NBDs (9, 10) or full ATP binding cassette (ABC) transporters (11–13). The ATP removal resulted in rapid opening in the NBDs of the maltose transporter (12), and the opening propagates to the intracellular side of the transmembrane domains (TMDs) due to the tight coupling between NBDs and the TMDs (12) (Fig. S2). Although no large-scale conformational changes can be observed in the whole TMDs, the NBD opening results in the formation of a cleft on the cytoplasmic side of the TMDs, which is followed by intermittent water permeation events (Fig. 4; Fig. S2). However, a set of control simulations of the same system under ATP-bound conditions (12) resulted in no NBD opening and tightly sealed intracellular gate of the TMDs (Fig. S2), and thus no water permeation through the transporter, suggesting that the water permeation in the maltose transporter is only accompanied with the conformational transitions and does not occur in the OF state.

Substrate binding and protonation of a critical residue in glycerol-3-phosphate transporter. Starting from the crystal structure in *apo* IF-state (PDB ID code 1PW4) (14), glycerol-3-phosphate transporter (GlpT) attains the observed water-conducting state only after two mechanistically relevant events deemed to be necessary for the IF-to-OF transition, namely, substrate binding and protonation of a histidine located in the vicinity of the bound substrate.

The first event is spontaneous substrate binding (Fig. S3) and subsequent partial occlusion of the cytoplasmic side of GlpT [~0.8 Å increase in C_α rmsd of the transmembrane (TM) helices; Fig. S3]. The details of the simulation systems and the conformational changes observed in these simulations can be found elsewhere (15, 16).

The second event is the protonation of the binding site histidine (H165) located in the vicinity of the bound substrate. The protonation of H165, in response to changes in the local electrostatic environment of the binding site due to the proximity of the charged substrate, is considered as one of the key events triggering IF-to-OF transition (17, 18). We tested the effect of the protonation of H165 in a 200-ns-long simulation starting with the $G3P^{2-}$-bound GlpT; that is, the final state obtained from the substrate binding simulation explained above (Fig. S3). The resulting structural changes on the periplasmic side triggered the separation of the helices that seal the periplasmic side (~1 Å increase in C_α rmsd of the helices; Fig. S3). Though the transporter remains occluded to the substrate, the separation is large enough to form a water-conducting state.

Water permeation through an intermediate state of bacterial GlT homolog Glt_{ph}. For Glt_{ph}, we have performed MD simulations on all of the crystallographically solved states—namely, the OF state (19, 20), IF state (21), and intermediate state (22). Water permeation events for Glt_{ph} were observed only in the intermediate state in our simulations. During the simulation, a continuous water pathway was observed at the interface between the transport domain—specifically, helical hairpin 1 (HP1)—and the trimerization domain of the monomer in the intermediate state (Fig. 2). Local conformational fluctuations of HP1 appear to accompany the formation of the water-conducting state (Fig. S4). We have also monitored the dynamics of Glt_{ph} in its IF state as well as its OF state (23, 24), and no water-conducting state was observed in

these states. The intermediate state is the only conformation exhibiting water permeation. This observation is consistent with experiments reporting that the Glt_{ph} is water permeable in its intermediate state (25).

Influence of the Substrate on Water Permeation in vSGLT. The presence of the substrate in vSGLT does not appear to significantly affect water permeation through the protein. In the 1.15-μs equilibrium MD simulation performed for vSGLT in its IF substrate-bound state (PDB ID code 3DH4) (26), we observed a large number of water permeation events, but no biased water flux across the membrane in either direction (Fig. 4; Fig. S5). The substrate exhibits significant displacement within the transporter lumen but does not fully release into the cytoplasmic side during the simulation (Fig. S5). The time series of water flux in either direction and the rmsd of the substrate do not show a clear correlation (Fig. S5). During the motion of the substrate toward the cytoplasmic side, the aqueous pathway remains unblocked, and water flux bypasses the substrate and continues to take place simultaneously in both directions. Therefore, there is no evidence from the simulations to support the proposed Brownian piston mechanism in vSGLT, in which the flux of the substrate would be accompanied by the flux of water molecules (27).

Additionally, we have performed a 450-ns simulation for vSGLT in a substrate-free IF state, and observed water permeation events and water-conducting states (Fig. S6) similar to those in substrate-bound IF-state simulations. Water molecules permeate along the putative substrate translocation pathway, and the radius of the constriction point of this pore is much smaller than that of the substrate as well. In addition, similar to substrate-bound vSGLT, the formation of water-conducting state and corresponding water permeation is a result of local conformational changes of the gating network at the extracellular side, i.e., the side chains of Y87, F424, and Q428 (Fig. S6). These residues are conserved in mammalian SGLTs, so one might expect a similar gating behavior for these side chains also in mammalian proteins.

SI Materials and Methods

System Setup and Simulation Protocol. A summary of the studied transporters is provided in Table 1. All of the transporter proteins were simulated in the explicit presence of membrane, water, and ions. The protein was inserted into a patch of lipid bilayer generated using the Membrane Builder plug-in of VMD (28), with the membrane normal aligned along the z axis. The lipid molecules overlapping with the protein were removed. The systems were then fully solvated using the program SOLVATE (29). NaCl was used to neutralize the systems and to bring the ionic concentration to ∼200 mM.

Simulations were performed using NAMD 2.6 (30) or Desmond on Anton (31), using the CHARMM force field (32) for proteins, lipids, ions, and substrate–galactose (33), and TIP3P model for explicit water (34). All simulations were performed under periodic boundary conditions with a time step of 2 fs. Throughout the simulations, bond distances involving hydrogen atoms were constrained using the SHAKE algorithm (35). After initial minimization of at least 1,000 steps, all systems were simulated using the following protocol: (*i*) 0.5-ns constant volume and constant temperature (NVT) simulation with all atoms constrained, except for the acyl chains of the lipid molecules, to introduce a higher degree of disorder in the lipid tails; (*ii*) simulation in a constant pressure and constant temperature (NPT) ensemble with positional restraints applied to all protein and substrate atoms; and (*iii*) equilibration in an NPT ensemble, without restraints. After the initial equilibration, the systems were subjected to production simulations in the NPT ensemble (Table 1). For MD simulations using NAMD, constant temperature was maintained by using Langevin dynamics with a damping coefficient of 0.5 ps^{-1}. The Langevin piston method (36, 37) was used to maintain a constant pressure of 1.0 atm with a piston period of 100 fs. Short-range nonbonded interactions were calculated using a cutoff distance of 12 Å, and long-range electrostatic interactions were calculated using the particle-mesh Ewald method (38). For MD simulations using Desmond on Anton (31), the Berendsen coupling scheme was used to maintain a constant pressure of 1.0 atm, and long-range electrostatic interactions were computed using the k-space Gaussian split Ewald method, with a $64 \times 64 \times 64$ grid.

Quantifying Water Permeation and Osmotic Permeability. Only full permeation events are counted, i.e., a water molecule has to traverse the entire membrane span to be counted as a permeation event. Quantification is done by defining two planes parallel to the membrane and positioned at different points along the membrane normal, with one on the cytoplasmic side and the other on the periplasmic/extracellular side in a way that they cover the entire lumen region of the transporter. The planes are about 25–30 Å apart, depending on the transporter system. For a water permeation event to take place, a water molecule needs to have crossed the membrane and both planes, i.e., traveling from one side of the membrane all of the way to the other side. The analysis is confined to a cylindrical region covering the lumen of the protein, and therefore excluding any possible water leak through the lipid bilayer.

Because there is no osmotic concentration gradient across the membrane in our simulation, we estimated the osmotic permeability (P_f) by using the theory developed by Zhu et al. (39) in which P_f is related to change in the square of the number of permeation events determined from an equilibrium simulation.

1. Weyand S, et al. (2008) Structure and molecular mechanism of a nucleobase-cation-symport-1 family transporter. *Science* 322(5902):709–713.
2. Zhao Y, et al. (2011) Substrate-modulated gating dynamics in a Na^+-coupled neurotransmitter transporter homologue. *Nature* 474(7349):109–113.
3. Claxton DP, et al. (2010) Ion/substrate-dependent conformational dynamics of a bacterial homolog of neurotransmitter:sodium symporters. *Nat Struct Mol Biol* 17(7):822–829.
4. Oldham ML, Khare D, Quiocho FA, Davidson AL, Chen J (2007) Crystal structure of a catalytic intermediate of the maltose transporter. *Nature* 450(7169):515–521.
5. Khare D, Oldham ML, Orelle C, Davidson AL, Chen J (2009) Alternating access in maltose transporter mediated by rigid-body rotations. *Mol Cell* 33(4):528–536.
6. Oldham ML, Chen J (2011) Crystal structure of the maltose transporter in a pretranslocation intermediate state. *Science* 332(6034):1202–1205.
7. Oldham ML, Chen J (2011) Snapshots of the maltose transporter during ATP hydrolysis. *Proc Natl Acad Sci USA* 108(37):15152–15156.
8. Chen J, Lu G, Lin J, Davidson AL, Quiocho FA (2003) A tweezers-like motion of the ATP-binding cassette dimer in an ABC transport cycle. *Mol Cell* 12(3):651–661.
9. Oloo EO, Fung EY, Tieleman DP (2006) The dynamics of the MgATP-driven closure of MalK, the energy-transducing subunit of the maltose ABC transporter. *J Biol Chem* 281(38):28397–28407.
10. Newstead S, et al. (2009) Insights into how nucleotide-binding domains power ABC transport. *Structure* 17(9):1213–1222.
11. Becker JP, Van Bambeke F, Tulkens PM, Prévost M (2010) Dynamics and structural changes induced by ATP binding in SAV1866, a bacterial ABC exporter. *J Phys Chem B* 114(48):15948–15957.
12. Wen PC, Tajkhorshid E (2011) Conformational coupling of the nucleotide-binding and the transmembrane domains in ABC transporters. *Biophys J* 101(3):680–690.
13. St-Pierre JF, Bunker A, Róg T, Karttunen M, Mousseau N (2012) Molecular dynamics simulations of the bacterial ABC transporter SAV1866 in the closed form. *J Phys Chem B* 116(9):2934–2942.
14. Huang Y, Lemieux MJ, Song J, Auer M, Wang DN (2003) Structure and mechanism of the glycerol-3-phosphate transporter from *Escherichia coli*. *Science* 301(5633):616–620.
15. Enkavi G, Tajkhorshid E (2010) Simulation of spontaneous substrate binding revealing the binding pathway and mechanism and initial conformational response of GlpT. *Biochemistry* 49(6):1105–1114.
16. Law CJ, Enkavi G, Wang DN, Tajkhorshid E (2009) Structural basis of substrate selectivity in the glycerol-3-phosphate:phosphate antiporter GlpT. *Biophys J* 97(5):1346–1353.
17. Law CJ, et al. (2008) Salt-bridge dynamics control substrate-induced conformational change in the membrane transporter GlpT. *J Mol Biol* 378(4):828–839.

18. Law CJ, Maloney PC, Wang DN (2008) Ins and outs of major facilitator superfamily antiporters. *Annu Rev Microbiol* 62:289–305.
19. Yernool D, Boudker O, Jin Y, Gouaux E (2004) Structure of a glutamate transporter homologue from *Pyrococcus horikoshii*. *Nature* 431(7010):811–818.
20. Boudker O, Ryan RM, Yernool D, Shimamoto K, Gouaux E (2007) Coupling substrate and ion binding to extracellular gate of a sodium-dependent aspartate transporter. *Nature* 445(7126):387–393.
21. Reyes N, Ginter C, Boudker O (2009) Transport mechanism of a bacterial homologue of glutamate transporters. *Nature* 462(7275):880–885.
22. Verdon G, Boudker O (2012) Crystal structure of an asymmetric trimer of a bacterial glutamate transporter homolog. *Nat Struct Mol Biol* 19(3):355–357.
23. Huang Z, Tajkhorshid E (2008) Dynamics of the extracellular gate and ion-substrate coupling in the glutamate transporter. *Biophys J* 95(5):2292–2300.
24. Huang Z, Tajkhorshid E (2010) Identification of the third Na^+ site and the sequence of extracellular binding events in the glutamate transporter. *Biophys J* 99(5):1416–1425.
25. Vandenberg RJ, Handford CA, Campbell EM, Ryan RM, Yool AJ (2011) Water and urea permeation pathways of the human excitatory amino acid transporter EAAT1. *Biochem J* 439(2):333–340.
26. Faham S, et al. (2008) The crystal structure of a sodium galactose transporter reveals mechanistic insights into Na^+/sugar symport. *Science* 321(5890):810–814.
27. Choe S, Rosenberg JM, Abramson J, Wright EM, Grabe M (2010) Water permeation through the sodium-dependent galactose cotransporter vSGLT. *Biophys J* 99(7): L56–L58.
28. Humphrey W, Dalke A, Schulten K (1996) VMD: Visual molecular dynamics. *J Mol Graph* 14(1):33–38, 27–28.
29. Grubmüller H (1996) Solvate 1.0. Available at www.unav.es/organica/umm/manuales/solvate/docu_html/docu.html.
30. Phillips JC, et al. (2005) Scalable molecular dynamics with NAMD. *J Comput Chem* 26(16):1781–1802.
31. Shaw DE, et al. (2009) Millisecond-scale molecular dynamics simulations on Anton. *SC '09: Proceedings of the Conference on High Performance Computing Networking, Storage and Analysis* (Assoc for Computing Machinery, Portland, OR), pp 39:1–39:11.
32. MacKerell AD, Jr., et al. (1998) All-atom empirical potential for molecular modeling and dynamics studies of proteins. *J Phys Chem B* 102(18):3586–3616.
33. Kuttel M, Brady JW, Naidoo KJ (2002) Carbohydrate solution simulations: Producing a force field with experimentally consistent primary alcohol rotational frequencies and populations. *J Comput Chem* 23(13):1236–1243.
34. Jorgensen WL, Chandrasekhar J, Madura JD, Impey RW, Klein ML (1983) Comparison of simple potential functions for simulating liquid water. *J Chem Phys* 79(2):926–935.
35. Ryckaert JP, Ciccotti G, Berendsen HJC (1977) Numerical integration of the Cartesian equations of motion of a system with constraints: Molecular dynamics of *n*-alkanes. *J Comput Phys* 23(3):327–341.
36. Martyna GJ, Tobias DJ, Klein ML (1994) Constant pressure molecular dynamics algorithms. *J Chem Phys* 101(5):4177–4189.
37. Feller SE, Zhang Y, Pastor RW, Brooks BR (1995) Constant pressure molecular dynamics simulation: The Langevin piston method. *J Chem Phys* 103(11):4613–4621.
38. Darden T, York D, Pedersen LG (1993) Particle mesh Ewald: An *N*·log(*N*) method for Ewald sums in large systems. *J Chem Phys* 98(12):10089–10092.
39. Zhu F, Tajkhorshid E, Schulten K (2004) Collective diffusion model for water permeation through microscopic channels. *Phys Rev Lett* 93:224501.

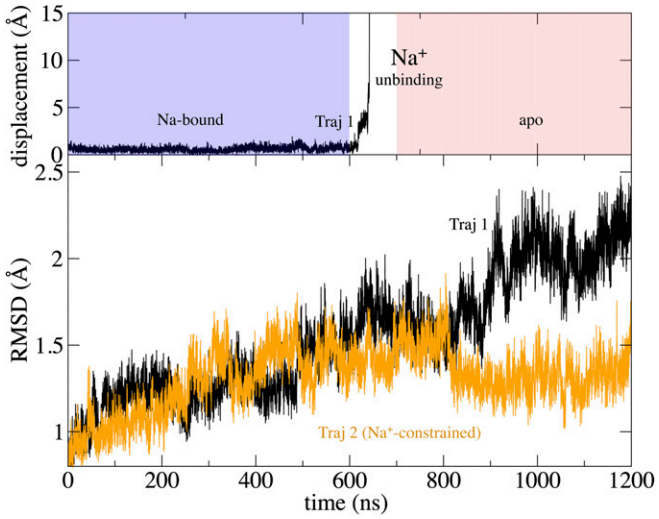

Fig. S1. Spontaneous Na^+ unbinding and conformational changes in Mhp1. (*Upper*) Displacement of Na^+ with respect to its original position in the Na^+ binding site. (*Lower*) C_α rmsd of the TM region of Mhp1 in Traj 1 (black) and Traj 2 with Na^+ constrained (orange).

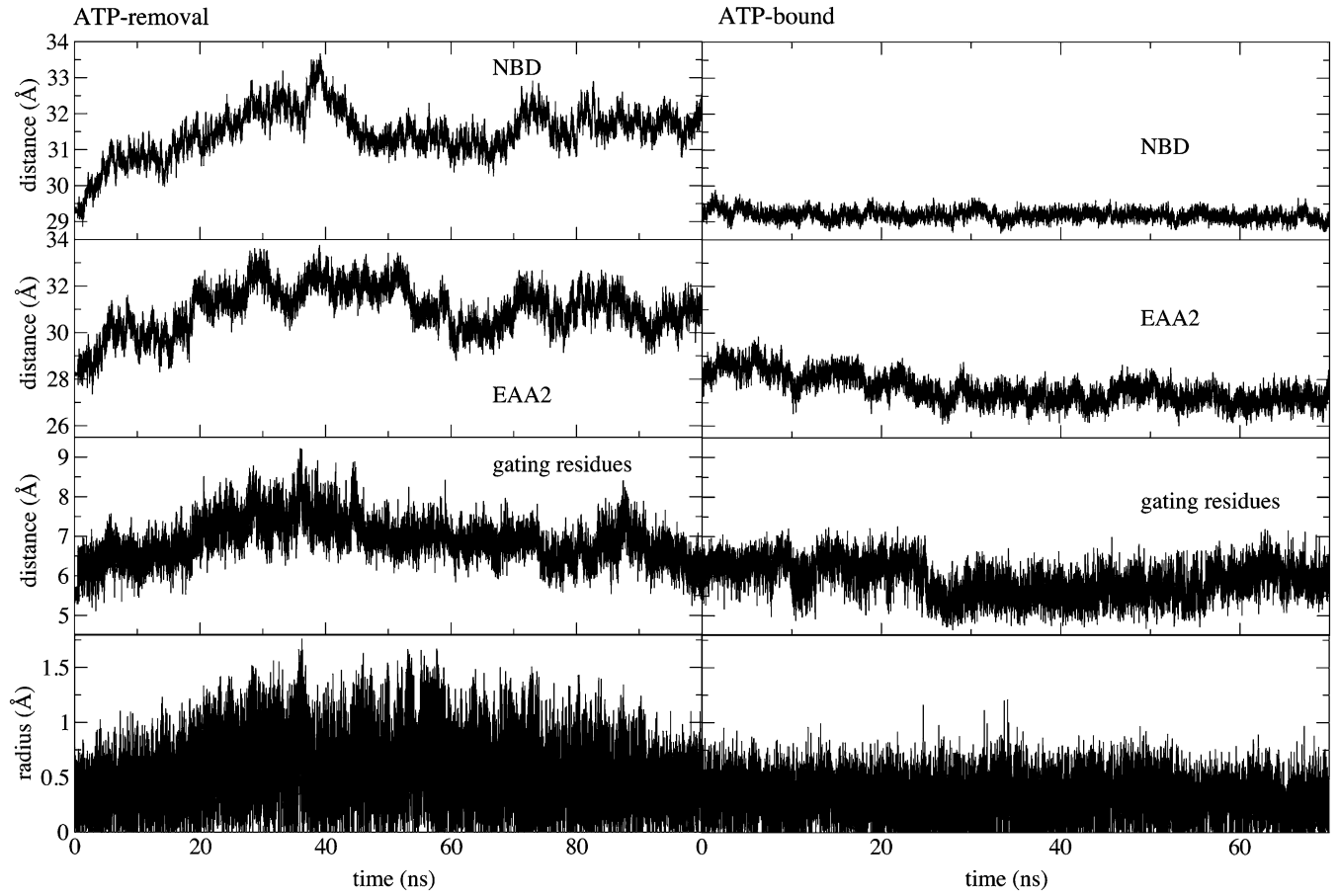

Fig. S2. Conformational changes in the maltose transporter that lead to water permeation. Conformational changes in the transporter are represented with several distances that differ between the system with ATP removed at $t = 0$ (*Left*) and the ATP-bound control simulation system (*Right*), listing from top to bottom: the center-of-mass distance between the two NBDs; the center-of-mass distance between the two excitatory amino acid transporter 2 (EAA2) helices, which are one of the NBD–TMD coupling elements (12) located closest to the core of the TMDs; the C_β–C_β distance between L387 of chain F and T176 of chain G, which delineate the constriction site of the central pore (gating residues); and the radius of the central pore at the constriction site.

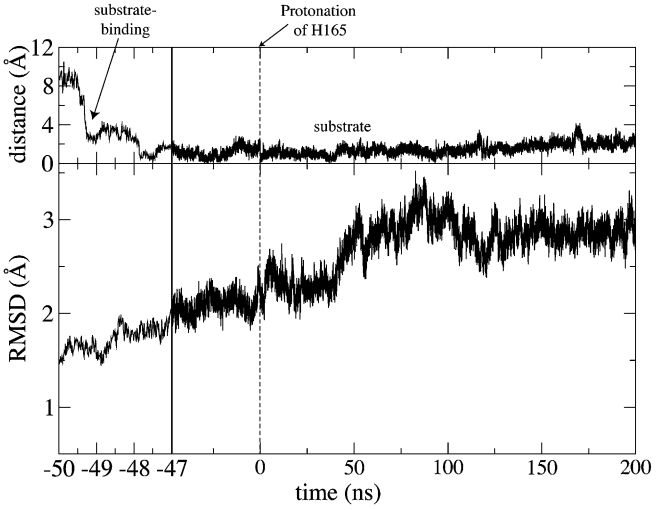

Fig. S3. Substrate binding and protonation of H165 result in conformational change in GlpT. (*Upper*) The distance of phosphorus atom of $G3P^{2-}$ to the binding site of GlpT (defined as the position of the phosphorus atom of $G3P^{2-}$ at $t = 0$ ns) as a function of time. (*Lower*) C_α rmsd of the transmembrane helices with respect to the crystal structure. The first 3 ns (−50 to −47 ns) of the simulation are shown in larger scale to show the substrate binding event clearly. The dashed line ($t = 0$ ns) indicates H165 protonation at N_ε.

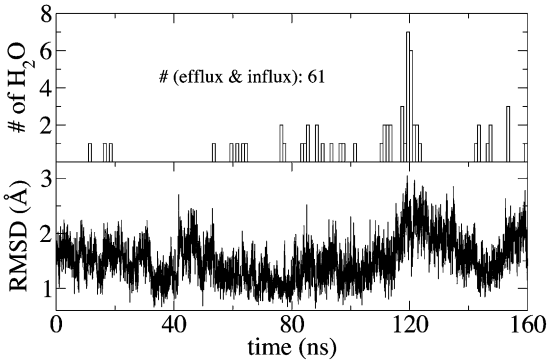

Fig. S4. Water permeation and dynamics of HP1 in the intermediate state of Glt_{ph}. (*Upper*) Water permeation events through the intermediate state. (*Lower*) The C_α rmsd of HP1 (residues 266–290) with reference to the intermediate crystal structure (PDB ID code 3V8G) (22).

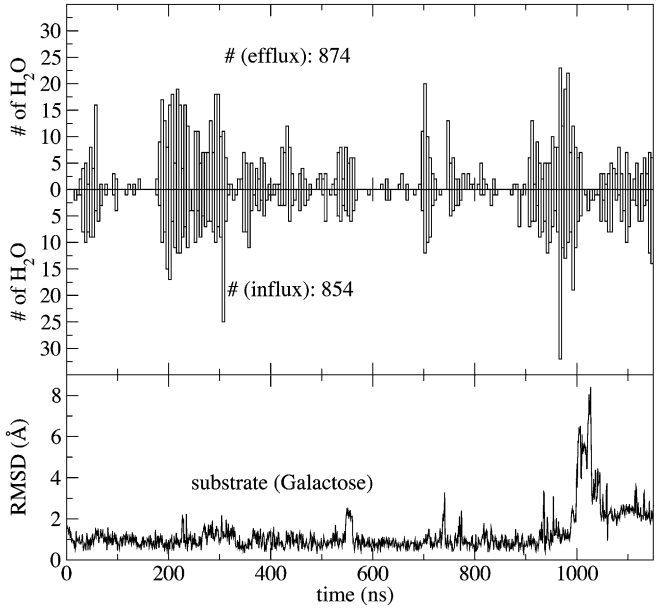

Fig. S5. Substrate motion and water permeation in vSGLT. The number of observed water permeation events in either direction (influx or efflux) is plotted against the simulation time (*Top* and *Middle*). (*Bottom*) Heavy-atom rmsd of the substrate (galactose).

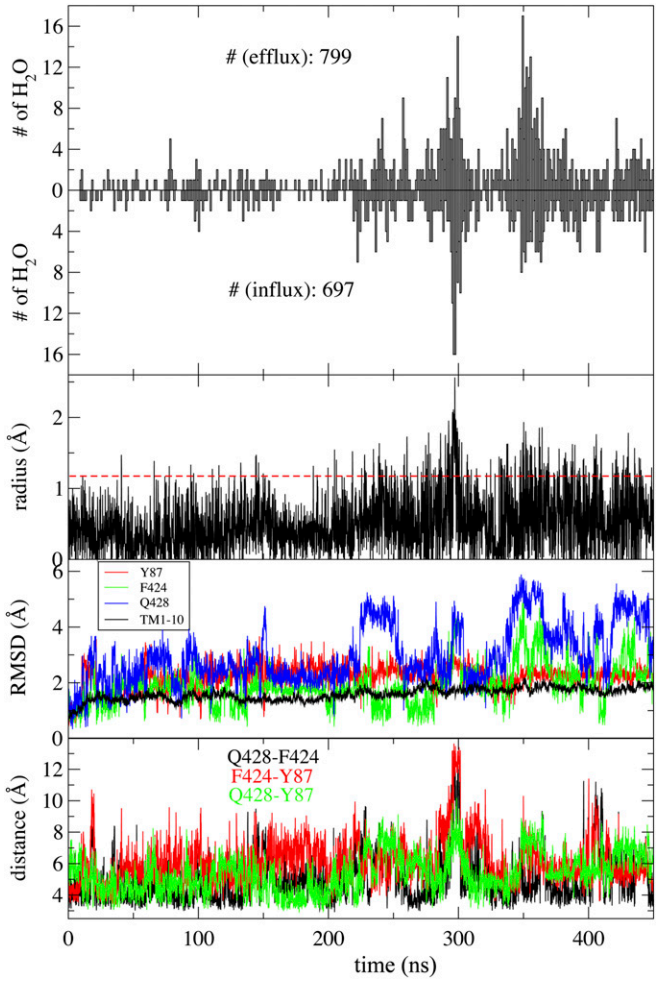

Fig. S6. Water permeation and protein dynamics in vSGLT in the absence of the substrate. The number of observed water permeation events in either direction (influx or efflux) is plotted against the simulation time in the top two panels. The third panel depicts the time series of the minimum radius of the aqueous pore. The fourth panel shows the rmsd of gating residues and the core transmembrane domain (10 TMs). The bottom panel shows the time evolution of the distances between the gating residues, i.e., Q428:$N_{\varepsilon 2}$–F424:$C_{\varepsilon 2}$, F424:$C_{\varepsilon 2}$–Y87:$C_{\varepsilon 1}$, and Q428:$N_{\varepsilon 2}$–Y87:$C_{\varepsilon 1}$.